n-hourglass Weyl fermions in nonsymmorphic materials

Yijie Zeng, Luyang Wang,* and Dao-Xin Yao†
State Key Laboratory of Optoelectronic Materials and Technologies, School of Physics, Sun Yat-Sen University, Guangzhou 510275, China

(Received 31 January 2019; revised manuscript received 12 January 2020; accepted 24 February 2020; published 9 March 2020)

Hourglasslike band structures protected by nonsymmorphic space group symmetries can appear along the high-symmetry lines or on the high-symmetry surfaces of the Brillouin zone. In this work, from symmetry analysis, we demonstrate that *n*-hourglasslike band structures, a generalization of hourglasslike band structures, are enforced along screw-invariant lines in nonmagnetic materials with an N-fold screw axis when spin-orbit coupling is finite, where n, a nonunity factor of N, denotes the degree of the screw-invariant line. The *n*-hourglass has a minimum of $n-1$ crossings, which are Weyl points with monopole charge ± 1. Using compatibility relations, we identify all the space groups that host *n*-hourglasslike band structures induced by screw symmetries, with $n = 2, 3, 4$. For $N = 3$ we find Weyl points that are *indirectly* enforced by symmetries. We construct an effective model, from which we see how the *n*-hourglasses appear when spin-orbit coupling is turned on. As examples, BiPd, the cinnabar phase of HgTe, and the high-temperature phase of Tl_3PbBr_5 are shown from first-principles calculations to exhibit *n*-hourglasslike band structures, with $N = 2, 3, 4$, respectively, which confirms our symmetry analysis. For $N = 3$ and 4, there are minimally two particle and two hole Fermi pockets enclosing Weyl points at proper fillings, where submanifold nesting may lead to topological density waves.

DOI: 10.1103/PhysRevB.101.115110

I. INTRODUCTION

The interplay between symmetry and topology has been a hot topic in condensed matter physics in recent years, stimulated by the discovery of topological insulators [1,2]. Topological insulators have been classified in the tenfold way according to whether they respect time-reversal symmetry (TRS), particle-hole symmetry, and chiral symmetry [3,4]. The discovery of topological crystalline insulators [5] has led to the realization that crystalline symmetries can vastly enrich topological phases. For crystalline solids with topological degeneracies, by digging into the 230 space groups (SGs), fermions beyond the Weyl-Dirac-Majorana classification have been found [6], and the filling constraints of semimetals in each SG have been presented [7].

Nonsymmorphic SG symmetries play a special role in the study of topological phases. For gapped systems, nonsymmorphic topological insulators and superconductors are classified according to their nonsymmorphic symmetries [8]. In particular, the surface states of nonsymmorphic topological insulators show hourglasslike dispersions [9]. The hourglasslike dispersions also appear in the bulk Brillouin zone (BZ) of nonsymmorphic materials with glide planes or twofold screw axes [10], and may result in nodal points [11,12], nodal lines [11,13,14], nodal chains [15,16], nodal nets [17,18], and nodal surfaces [19]. However, the topological degeneracies in systems which have a screw axis with degrees more than two have not been well explored yet.

In this work we investigate the spin-orbit coupled crystalline solids which have an N-fold screw axis and respects TRS. By symmetry analysis, we find that the symmetries enforce *n*-hourglasslike dispersion along screw-invariant lines, which is a generalization of the hourglasslike dispersion. The integer n is a nonunity factor of N. An *n*-hourglass has at least $n-1$ symmetry-enforced band crossings, which are Weyl points (WPs). In this language, the conventional hourglass is a 2-hourglass, and 3-, 4-, and 6-hourglass can also appear in systems with screw symmetries. We notice that the $n = 6$ case has been considered in Ref. [20]. Here we identify all SGs with screw axes that host *n*-hourglasses with $n = 2, 3, 4$. An effective model is presented to produce the *n*-hourglasslike dispersion for an arbitrary n. Moreover, we perform first-principles band structure calculations on materials with screw symmetries, showing results consistent with our symmetry analysis. Specifically for $N = 3$, we identify symmetry-indirectly-enforced WPs, which are neither accidental degeneracies nor degeneracies directly enforced by symmetries. Possible physical effects are discussed.

II. SYMMETRY ANALYSIS

We study nonmagnetic crystalline systems with an N-fold screw axis ($N = 2, 3, 4$) and sizable spin-orbit coupling (SOC). We use a shorthand notation $\widetilde{C}_N^p$ to denote the screw operation $\{C_{Nz}|\frac{p}{N}\hat{\mathbf{z}}\}$, where $p = 1, 2, \ldots, N-1$. The screw axis is assumed to be along z direction and the lattice constant is set to be 1.

We first focus on systems invariant under screw rotation $\widetilde{C}_N^1$. In the BZ there are high symmetry lines left invariant by an n-fold screw $\widetilde{C}_n^1$ [see Figs. 1(a)–1(c)], where $1 < n \leqslant N$ is a factor of N. Along a screw-invariant line, the

*wangluyang730@gmail.com
†yaodaox@mail.sysu.edu.cn

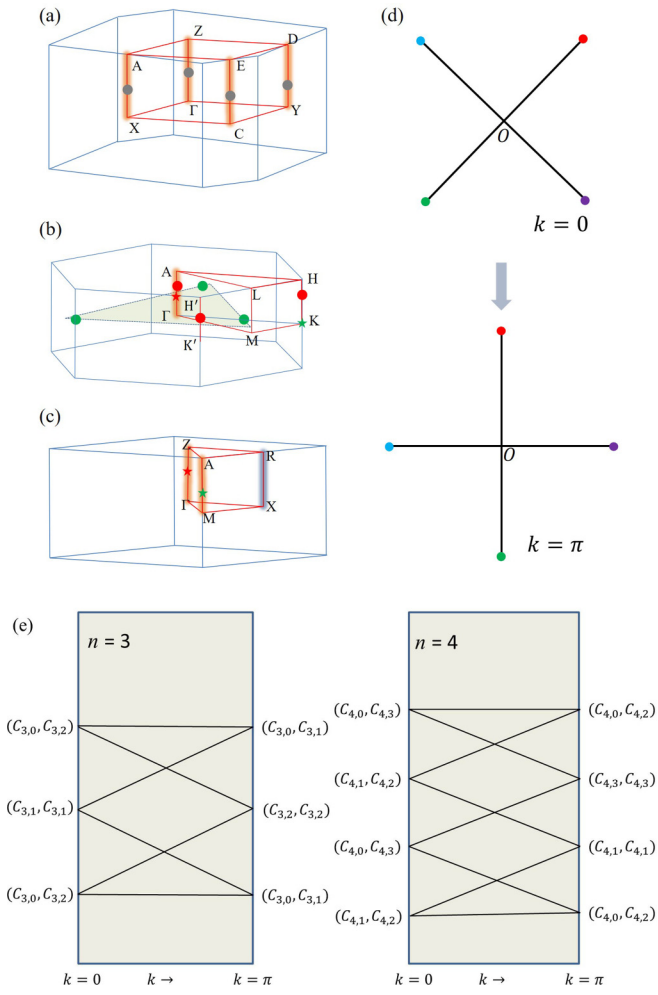

FIG. 1. (a-)–(c) The BZ of SG $P2_1$ (a), $P3_1$ (b), and $P4_1$ (c), which belong to the primitive monoclinic, hexagonal, and primitive tetragonal Bravais lattice, respectively. (d) Eigenvalues of the screw rotation $\widetilde{C}_4^1$ at $k = 0$ and π shown in the complex plane. They are rotated by $\pi/4$ when k goes from 0 to π. (e) Schematic of how the n-hourglass results from different patterns of Kramers pairing at $k = 0$ and π, for $n = 3$ and $n = 4$.

bands can be labeled by screw eigenvalues. Consider an n-fold screw-invariant line in the BZ ended with time-reversal invariant momenta (TRIM). Since n times of $\widetilde{C}_n^1$ translate the system by a unit cell along the screw axis, we have $(\widetilde{C}_n^1)^n = -e^{ik}$ in Bloch wave basis, where k is the wave vector in z direction, and the minus sign accounts for the rotation of spin-1/2. Therefore, the eigenvalues of $\widetilde{C}_n^1$ are $C_{n,m}(k) = e^{\frac{i(k+\pi)+i2\pi m}{n}}$, with $m = 0, 1, \ldots, n-1$. They are rotated by $\frac{\pi}{n}$ in the complex plane when k goes from 0 to π, as shown in Fig. 1(d) for $n = 4$. TRS imposes Kramers degeneracies at TRIM, where states with screw eigenvalues conjugate with each other to form Kramers pairs. Therefore, at $k = 0$, a state with screw eigenvalue $C_{n,m}$ pairs with another one with $C_{n,n-m-1}$, while at $k = \pi$, a state with $C_{n,m}$ pairs with another with $C_{n,n-m-2}$. The switching of Kramers partners results in the band structures illustrated in Fig. 1(e) for $n = 3$ and 4, which we call n-hourglasslike band structures, where $2n$ bands stick together with at least $n-1$ symmetry-enforced band crossings. In Appendix A we show how the n-hourglasslike band structures are formed for a generic n. The same results can also be derived from the compatibility relations between the irreducible representations of the little group of different wave vectors, see Appendix C for details. If the symmetry operation of a system is $\widetilde{C}_N^{N-1}$, similar analysis again shows that n-hourglasses appear along n-fold screw-invariant lines. But for $\widetilde{C}_4^2$, only 2-hourglasses appear.

Note that all crossings in the n-hourglass are WPs [21] in three-dimensional systems. The Kramers pairs at $k = 0$ are also WPs, but those at $k = \pi$ are WPs only if N is odd. For an even N, double degeneracy occurs in the whole $k = \pi$ plane due to the antiunitary symmetry $T(\widetilde{C}_N^1)^{N/2}$ which leaves a generic point in the plane invariant and squares to -1, resulting in a nodal surface.

The SGs with the only symmetry operation $\widetilde{C}_N^1$ or $\widetilde{C}_N^{N-1}$ are $P2_1$, $P3_1$, and $P3_2$, and $P4_1$ and $P4_3$ for $N = 2, 3, 4$, respectively. Their BZs are shown in Figs. 1(a)–1(c), where the high symmetry points and lines are highlighted. The screw-invariant lines ended with TRIM are shaded, along which n-hourglasses are enforced. Note that for $N = 4$ which has two nonunity factors, there are both fourfold screw-invariant lines (ΓZ and MA) along which 4-hourglasses appear and a twofold screw-invariant line (XR) along which 2-hourglasses appear. For $N = 3$, $KH(K'H')$ is screw-invariant, but $K(K')$ and $H(H')$ are not TRIM, so crossings seem not guaranteed. However, we will show later that band crossings are indirectly enforced by symmetries along $KH(K'H')$ as well as inside the BZ.

To figure out whether the n-hourglasslike dispersions survive if other symmetry elements besides the N-fold screw axis are present, we examine the compatibility relations between the irreducible representations of little groups of different wave vectors. We find that if there are twofold rotation or twofold screw axes perpendicular to the N-fold screw axis, the n-hourglasses will be preserved; if there are mirror or glide planes whose normal is perpendicular to the N-fold screw axis, the n-hourglasses will disappear along certain or all screw-invariant lines. The SGs hosting n-hourglasses with $n = 2, 3, 4$ are listed in Table I.

III. SYMMETRY-INDIRECTLY-ENFORCED WEYL POINTS

Band crossings can usually be divided into two classes, accidental ones or symmetry-enforced ones. Now we show that band crossings that are neither accidental nor directly enforced by symmetries exist in systems with a threefold screw axis. For $N = 3$, there is only one screw-invariant line ΓA ended with two TRIM. Therefore, there is minimally one symmetry-enforced WP along ΓA as the crossing between, for example, the second and the third highest band in a 3-hourglass. (Only the upper half of the BZ is considered, since the lower half is related by TRS.) Due to the fermion doubling theorem [23], there must exist an odd number of other WPs for the cancellation of the total monopole charge. The threefold symmetry tells us that WPs could triply appear with the same charge if located inside the BZ, which cannot make the total charge vanish. If the WPs are located at the surface of the BZ, a triple set contributes charge $\pm 3/2$, which is also unsatisfactory. Therefore, the only possibility is that

TABLE I. List of SGs that host n-hourglasslike dispersions, with the screw-invariant lines given. The SGs are classified by symmetry elements in addition to the N-fold screw axis: twofold rotation axes ($\perp 2$) or twofold screw axes ($\perp 2_1$) perpendicular to the N-fold screw axis, a mirror/glide plane whose normal is perpendicular to it (m), or none of them (None). The high symmetry points for the Brillouin zone are given in Ref. [22].

n	None	$\perp 2$	$\perp 2_1$	m
2	$P2_1(\Gamma Z, XA, YD, CE)$, $P4_2(\Gamma Z, XR, MA)$, $P6_3(\Gamma A)$, $I4_1(\Gamma Z)$	$P222_1(\Gamma Z, XU, YT, SR)$, $P42_12(\Gamma X)$, $P4_222(\Gamma Z, MA)$, $P6_322(\Gamma A)$, $C222_1(\Gamma Z, YT, SR)$, $I4_122(\Gamma Z)$	$P2_12_12(\Gamma X, ZU, \Gamma Y, ZT)$, $P2_12_12_1(\Gamma X, \Gamma Y, \Gamma Z)$, $P4_22_12(\Gamma Z, \Gamma X)$, $P2_13(\Gamma X)$, $P4_232(\Gamma X)$, $F4_132(\Gamma X)$, $I4_132(\Gamma H)$, $P4_132(\Gamma X)$, $P4_332(\Gamma X)$	$Pca2_1(XU, SR)$, $Pmn2_1(XU, SR)$, $Pna2_1(XU, YT)$, $P4_2nm(XR)$, $P4_2bc(MA)$, $P\bar{4}2_1m(\Gamma X)$, $P\bar{4}2_1c(\Gamma X)$, $Cmc2_1(SR)$
3	$P3_1(\Gamma A)$, $P3_2(\Gamma A)$, $P6_2(\Gamma A)$, $P6_4(\Gamma A)$	$P3_112(\Gamma A)$, $P3_121(\Gamma A)$, $P3_212(\Gamma A)$, $P3_221(\Gamma A)$, $P6_222(\Gamma A)$, $P6_422(\Gamma A)$		
4	$P4_1(\Gamma Z, MA)$, $P4_3(\Gamma Z, MA)$	$P4_122(\Gamma Z, MA)$, $P4_322(\Gamma Z, MA)$	$P4_12_12(\Gamma Z)$, $P4_32_12(\Gamma Z)$	

the other(s) is at another screw-invariant line KH or $K'H'$, or both. Then there are two possible cases: (i) One other WP is located at KH *or* $K'H'$, which we call the $1+1$ case. (ii) Two other WPs are located at KH and $K'H'$, and then there must be a triple set of WPs inside the BZ to cancel out the total charge, which we call the $3+3$ case. The two cases are indicated by the stars and dots in Fig. 1(b), colored differently for opposite charges. Different from symmetry-enforced WPs in an n-hourglass and accidental WPs, the WPs at $KH/K'H'$ and inside the BZ are *indirectly* enforced by symmetries.

The $1+1$ case can also occur in SG $P4_1$ and $P4_3$, as indicated by the stars in Fig. 1(c). The symmetry-enforced WPs between the fourth and the fifth highest band in a 4-hourglass are located at ΓZ and MA, but not at XR. The two WPs can carry opposite charges, leaving a zero net charge as required.

IV. EFFECTIVE MODEL FOR THE n-HOURGLASSLIKE DISPERSION

We develop an effective model for the n-hourglasslike dispersion for an arbitrary n, which reads

$$H_n(k) = S_n(k) + S_n^\dagger(k) + \lambda i[S_n(k) - S_n^\dagger(k)]\sigma_z, \qquad (1)$$

where σ_i denotes the Pauli matrices acting on spin, λ is a parameter characterizing the strength of SOC, and S_n is an n-dimensional matrix representing the n-fold screw rotation,

$$S_n = \begin{pmatrix} 0 & 0 & \dots & e^{ik} \\ 1 & 0 & \dots & 0 \\ & & & \\ 0 & \ddots & 0 & 0 \\ 0 & \dots & 1 & 0 \end{pmatrix}. \qquad (2)$$

$H_n(k)$ constructed in this way respects TRS and n-fold screw symmetry. In Fig. 2 we show how the n-hourglasses emerge for $n = 2, 3, 4$, upon the tuning of the SOC from zero to finiteness using this model. In Appendix E we present a tight-binding model, which at screw-invariant lines ended with TRIM agrees with the effective model.

V. MATERIALS REALIZATION

We perform first-principles band structure calculations on BiPd, the cinnabar phase of HgTe, and the high temperature phase of Tl_3PbBr_5, which belong to SG $P2_1$, $P3_121$, and $P4_1$, respectively. For details see Appendix B, including methods of calculations and the crystal structures and band structures of each material, and see Appendix D for band structures without SOC. In Fig. 3 we show the band structures of the three materials along screw-invariant lines, where n-hourglasses are seen with $n = 2, 3, 4$. In particular, we find symmetry-indirectly-enforced band crossings for HgTe, labeled by the blue dot in Fig. 3(b), accompanying the symmetry-enforced one labeled by the red dot.

To further confirm our analysis, we find all the crossings between the second and third highest bands below Fermi level for HgTe in cinnabar phase. The monopole charge of each crossing is found to be ± 1, so they are all WPs. We show their projection to the $k_z = 0$ plane in Fig. 4(a). There are totally 96 WPs in the BZ, and we reproduce the ones in the upper half BZ in Fig. 4(b), colored orange for monopole charge 1 and purple for -1. The three WPs projected to Γ, K, and K' carry charge 1, which have to be canceled out by a triple set of WPs with charge -1 inside the BZ, realizing the $3+3$

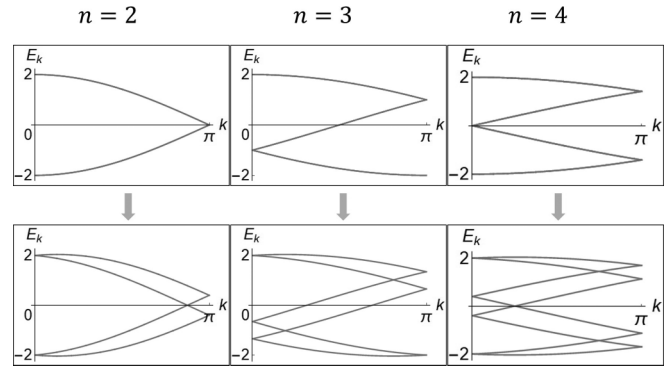

FIG. 2. Schematic of how n-hourglasses emerge for $n = 2, 3, 4$ when the SOC is turned on. $\alpha = 0$ in the upper plots and $\alpha = 0.2$ in the lower plots.

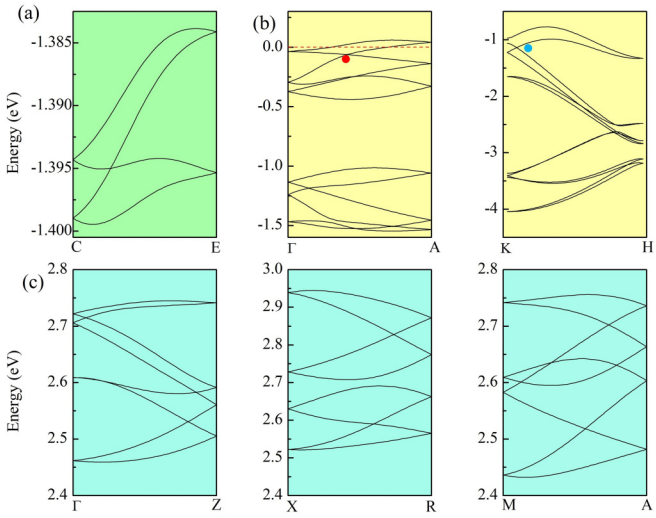

FIG. 3. The n-hourglasslike band structures near the Fermi energy along the screw-invariant lines for (a) BiPd, (b) HgTe, and (c) Tl_3PbBr_5. The blue dot labels a symmetry-indirectly-enforced WP, accompanying the symmetry-enforced one labeled by the red dot.

case discussed earlier. Other WPs are accidental degeneracies, the number of which (42) being a multiple of 6, due to the threefold symmetry and fermion doubling.

VI. PHYSICAL EFFECTS

Consider a system with a threefold screw symmetry at 1/3 or 2/3 filling, such that the Fermi energy is tuned to be near a crossing of the 3-hourglass along ΓA. We focus on the $1+1$ case and assume there are no accidental degeneracies. Since the two WPs are not related by symmetries, they are not at the same energy [24–26]. Therefore, the Fermi level is between the energies of the WPs, resulting in a particle and a hole Fermi pocket. The cross section of a Fermi pocket at a specific k_z has a threefold symmetry. But if the Fermi pocket is small, the trigonal warping can be neglected and the cross section is approximately a circle (like in graphene, see, e.g., Ref. [27]),

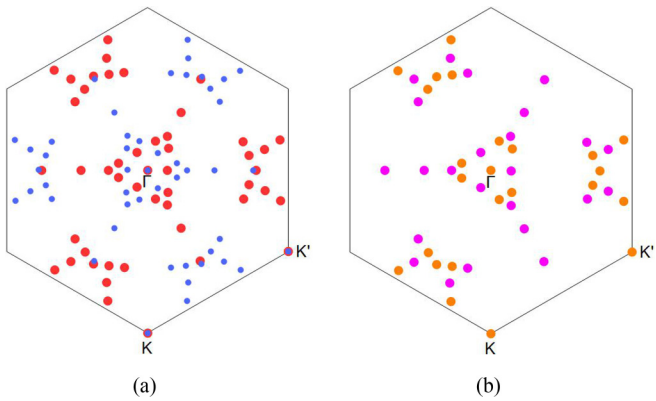

FIG. 4. (a) All 96 WPs as band crossings between the second and third highest bands of HgTe below Fermi level, projected to the $k_z = 0$ plane. Red ones are in the upper half BZ and blue ones in the lower half. (b) The 48 WPs in the upper half BZ, orange ones with monopole charge $+1$ and purple ones with -1.

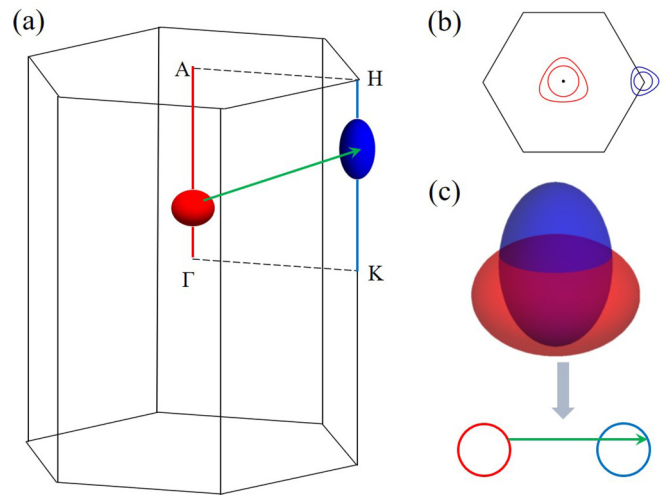

FIG. 5. (a) Two Fermi pockets, one electronlike and one holelike, at the two screw-invariant lines. Each pocket encloses a WP. (b) The projection of the two Fermi pockets on the plane perpendicular to the k_z axis at two different energies. The cross sections of the Fermi pockets have threefold rotational symmetry, but become circular if the Fermi pockets are small. (c) Schematic of how the nesting of Fermi surface submanifolds occurs. The green arrow in (a) indicate the nesting vector, whose projection is shown in (c), together with the projection of the nested Fermi surface submanifolds.

resulting in an ellipsoidal Fermi pocket, as shown in Figs. 5(a) and 5(b). Although there is not perfect nesting between the two ellipsoids, there must be nesting between submanifolds of them, as shown in Fig. 5(c), since the cross sections of the two Fermi pockets can be of the same size. When a repulsive interaction V is present, the effective interaction is $V_{\text{eff}} = V/[1 - V\Pi(\mathbf{q})]$, where $\Pi(\mathbf{q})$ is the polarization operator. The divergence of V_{eff} leads to density-wave instabilities. With perfect nesting, $\Pi(\mathbf{Q})$ has a logarithmic divergence where $\mathbf{Q}$ is the nesting vector, and an arbitrarily small V can induce density waves. Here, with only submanifold nesting, V has to be larger than a critical value V_c for instabilities to occur. The maximum of $\Pi(\mathbf{q})$ determines V_c and the wave vector $\mathbf{Q}$ of the resulting density wave. Detailed calculations of $\Pi(\mathbf{q})$ are beyond the scope of the present work and we give intuitive arguments here. In calculating $\Pi(\mathbf{q})$, the in-plane integral gives $N_{2D} \ln A/\Omega$, where A and Ω are respectively the high energy and low energy cutoff, and N_{2D} is the 2D density of states at the cross section. The integration over k_z kills the divergence. Intuitively, when the cross section is the largest, we have the largest N_{2D} and the system could be the most susceptible, from which $\mathbf{Q}$ (indicated by the green arrows in Fig. 5) is found. The density wave obtained has topological nature [28]. Although in general the ellipsoids are deformed since the Weyl cone is tilted in the z direction, the cross sections are still approximately circular and the above argument works. Similar arguments apply to the $1+1$ case for $N = 4$.

The materials in the SGs considered here preserve TRS and break inversion symmetry, thus cannot have the linear Hall effect. However, the tilted Weyl cones generate Berry curvature dipoles, which can lead to the quantum nonlinear Hall effect [29,30]. This effect should be readily observed in the materials with n-hourglass Weyl fermions.

VII. DISCUSSION

Although the three representative materials we have discussed host n-hourglass Weyl fermions, they are not filling-enforced semimetals [7]. To experimentally find the physical effects discussed, physical or chemical doping can be used to shift the Fermi energy towards the WPs, and searching for filling-enforced semimetals in the SGs specified is highly desired.

A future direction is to investigate the possible generalizations of the n-hourglasses to magnetic SGs, including the fermionic quasiparticle spectrum as well as the bosonic collective modes, magnons. As Weyl magnons have been found [31], magnons with n-hourglasslike dispersion may appear in certain magnetic SGs. Metamaterials such as photonic crystals [32] have proved to be a wonderful playground to realize topological phases, where we expect the n-hourglass WPs may also be engineered.

Note added—Recently, a work on symmetry-enforced band crossings in trigonal materials [33] appeared, with some results similar to our $N = 3$ case.

ACKNOWLEDGMENTS

L.W. thanks S.-K. Jian, H. Yao, Z. Yan, and P. Ye for useful discussions. This work was supported by NKRDPC-2017YFA0206203, NKRDPC-2018YFA0306001, NSFC-11974432, NSFG-2019A1515011337, National Supercomputer Center in Guangzhou, and Leading Talent Program of Guangdong Special Projects.

APPENDIX A: THE FORMATION OF n-HOURGLASSLIKE BAND STRUCTURES FOR A GENERIC n: GRAPH THEORETICAL DESCRIPTION

Graph theory has been applied to study the connectivity in band theory [34,35]. Here we present a graph-theoretical description on how the n-hourglasslike band structures are formed. Consider the screw rotation $\widetilde{C}_n^1$, a rotation by $2\pi/n$ about the screw axis combined with a translation $1/n$ parallel to the screw axis, where the lattice constant along the screw axis is assumed to be 1. Although n can only be 2, 3, 4, or 6 in a three-dimensional (3D) crystal, it can be any integer larger than 1 in a one-dimensional (1D) system, so we assume a generic $n > 1$. We use $C_{n,m}$ to label the eigenvalues of $\widetilde{C}_n^1$. Since n times of the screw operation translate the system by a unit cell along the screw axis, we have $(\widetilde{C}_n^1)^n = -e^{ik}$ where k is the wave vector in that direction, and the minus sign accounts for the rotation of spin-1/2. Therefore, the eigenvalues of $\widetilde{C}_n^1$ are $C_{n,m}(k) = e^{\frac{i(k+\pi)+i2\pi m}{n}}$, with $m = 0, 1, \ldots, n-1$. Due to time-reversal symmetry (TRS), time-reversal operation pairs the states with eigenvalues conjugate to each other at the time-reversal invariant momenta (TRIM). At $k = 0$, one state with screw eigenvalue $C_{n,m}(0)$ pairs with another with $C_{n,n-m-1}(0)$; while at $k = \pi$, one with $C_{n,m}(\pi)$ pairs with another with $C_{n,n-m-2}(\pi)$. This is illustrated in the left panel of Fig. 6, where $C_{n,m}(k)$ is written as C_m for short and m is equivalent to $m(\mathrm{mod}\, n)$. The dashed lines indicate the 0 pairing while the solid lines π pairing, where k pairing means the Kramers pairing at k. In graph theory, the lines are called edges and the points are called vertices. The two possibilities

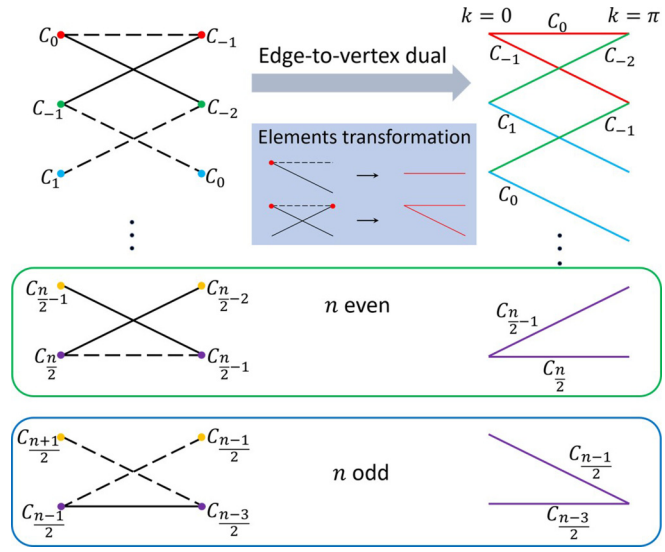

FIG. 6. Schematic of how the n-hourglass results from different patterns of Kramers pairing at $k = 0$ and π, for both n even and n odd. C_m means the m (mod n)th eigenvalue of $\widetilde{C}_n^1$, $C_{n,m}(k)$.

how the graph ends are shown, depending on whether n is even or odd. The sum of m of the two eigenvalues is $-1(\mathrm{mod}\, n)$ if the vertices are connected by dashed lines, and $-2(\mathrm{mod}\, n)$ by solid lines. Such pairing relations result in the dispersion shown in the right panel of Fig. 6 in the following way. Each vertex in the left panel is transformed into an edge in the right panel, with its color kept; and a dashed edge is transformed into a vertex at $k = 0$ while a solid edge is transformed into a vertex at $k = \pi$. This is like the edge-to-vertex dual (or the line graph) in graph theory, but with the constraint that the crossings of the original graph are not considered as vertices. We call the dual graph where $2n$ bands stick together the n-hourglasslike dispersion.

In graph-theoretical language, the n-hourglass is a (2,2)-biregular graph [36], i.e., the vertices are divided into two subsets with an equal cardinality n, and each vertex of both subsets has two incident edges. In the simplest case, the n-hourglass has $n - 1$ crossings, all of which are Weyl points in 3D systems. Along the screw-invariant lines which connect two TRIM, we call the TRIM near the center of the Brillouin zone (BZ) the inner edge of the n-hourglass, whereas the TRIM farther the outer edge. The n vertices at the inner edge of the n-hourglass are also Weyl points. However, the outer edge may not host Weyl points, depending on the value of n. For $n = 2$, it has been shown that the degeneracies at the outer edge reside on a nodal surface [11]. This also happens for $n = 4$. However, for $n = 3$, the degeneracies at the outer edge are Weyl points. Permutations of the vertices at the edges and curving the bands can introduce more Weyl points.

By similar reasoning, one can deduce that the screw symmetry $\widetilde{C}_n^{n-1}$ results in the same n-hourglasslike dispersions as $\widetilde{C}_n^1$.

APPENDIX B: THE FULL BAND STRUCTURES AND METHODS OF CALCULATION

Our first-principles calculations have been performed on BiPd, the cinnabar phase of HgTe, and the high temperature

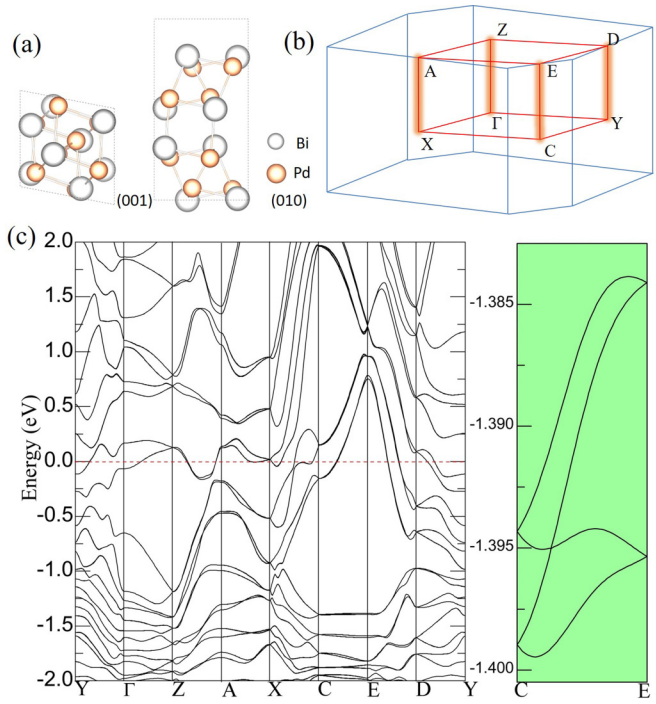

FIG. 7. (a) Crystal structure of BiPd in SG $P2_1$. (b) The first BZ and the high symmetry points and lines. The screw-invariant lines are highlighted by glowing orange. (c) Band structure of BiPd (with SOC). A 2-hourglass along CE is enlarged and shown on the right.

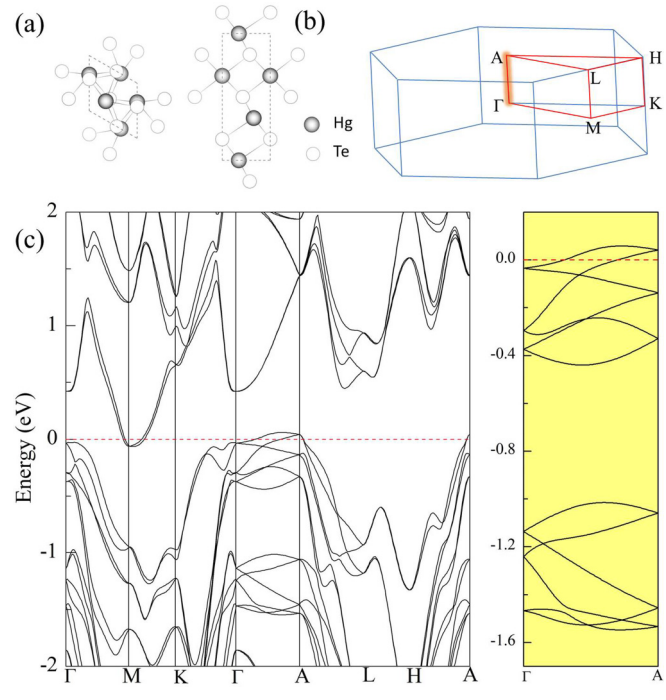

FIG. 8. (a) Crystal structure of HgTe in SG $P3_121$. (b) The first BZ and the high symmetry points and lines. The screw-invariant line ended with two TRIM is highlighted. (c) Band structure of HgTe (with SOC). The valence bands near Fermi energy showing 3-hourglass band crossings are enlarged and shown on the right.

phase of Tl_3PbBr_5, which possess an N-fold screw axis with $N = 2, 3, 4$, respectively, as well as TRS. The spin-orbit coupling (SOC) is expected to be sizable in these materials.

BiPd is a monoclinic crystal with 16 atoms in the unit cell. It becomes superconducting below 3.8 K [37] and a Dirac cone surface state exists on the (010) surface [38]. The band structure shows metallic behavior, with 12 bands crossing the Fermi energy. The SOC causes band splitting except at the eight TRIM where Kramers degeneracy appears. According to our symmetry analysis, the bands along the screw-invariant lines must show 2-hourglasslike dispersion. In Fig. 7 we show the full band structure of BiPd, and that along CE, a twofold screw-invariant line. It should be mentioned that all the bands, from the bottom valence bands to the top conduction bands, show similar behavior—every four bands form a 2-hourglass if the SOC is large enough.

HgTe is a IIB-VI semiconductor in zinc-blende (ZB) structure at ambient pressure, and turns into cinnabar phase at 1.4 GPa and further into rocksalt phase at 8 GPa [39–42]. Similar to BiPd, 3-hourglasslike dispersions are observed for the bands along the TRIM-ended screw-invariant line ΓA, as shown in Fig. 8. As discussed in the main text, in half of the BZ, the number of Weyl points as the crossings of the second and the third highest band below the Fermi energy realizes the $3 + 3$ case. The band structure calculations show that HgTe in cinnabar phase is a compensated semimetal, in which effects of the Weyl points should be observable.

Tl_3PbBr_5 can achieve effective doping of rare-earth element and can be applied as nonlinear optical devices [43]. Two phases are identified, the low-temperature orthorhombic phase [space group (SG) $P2_12_12_1$] and the high-temperature tetragonal phase (SG $P4_1$) [44], with transition temperature about 239 °C. For the high-temperature phase there are 36 atoms per unit cell. As shown in Fig. 9, 4-hourglasslike dispersions along the fourfold screw-invariant lines ΓZ and MA, and 2-hourglasslike dispersions along the twofold screw-invariant line XR, are observed. Since Tl_3PbBr_5 is an insulator, the underlying Weyl points can only be revealed upon physical or chemical doping.

Band structure calculations were performed by density functional theory using the Vienna *ab initio* simulation package (VASP) [45]. The projector augmented-wave (PAW) [46] pseudopotentials were used and the generalized gradient approximation of the PBE type functional [47] was used describing the exchange-correlation energy. A cutoff energy of 700 eV (500 eV for Tl_3PbBr_5) was used for the plane wave expansion to ensure the convergence of total energy to be less than 1 meV. The Monkhorst-Pack grid [48] for BZ sampling was set to $7 \times 7 \times 7$, $15 \times 15 \times 9$, and $7 \times 7 \times 5$ for BiPd, HgTe, and Tl_3PbBr_5, respectively. The structures were fully optimized with experimental lattice constants used, until the forces were smaller than 0.01 eV/Å.

APPENDIX C: COMPATIBILITY RELATIONS

The n-hourglasslike band structures in nonsymmorphic SGs can also be derived by considering the compatibility relations [20] between irreducible representations at different high symmetry points and lines. We derive the compatibility relations for $P4_1$ and $P3_1$ below. We will see that the n-hourglasses are automatically generated as a rigorous result of the symmetry requirement.

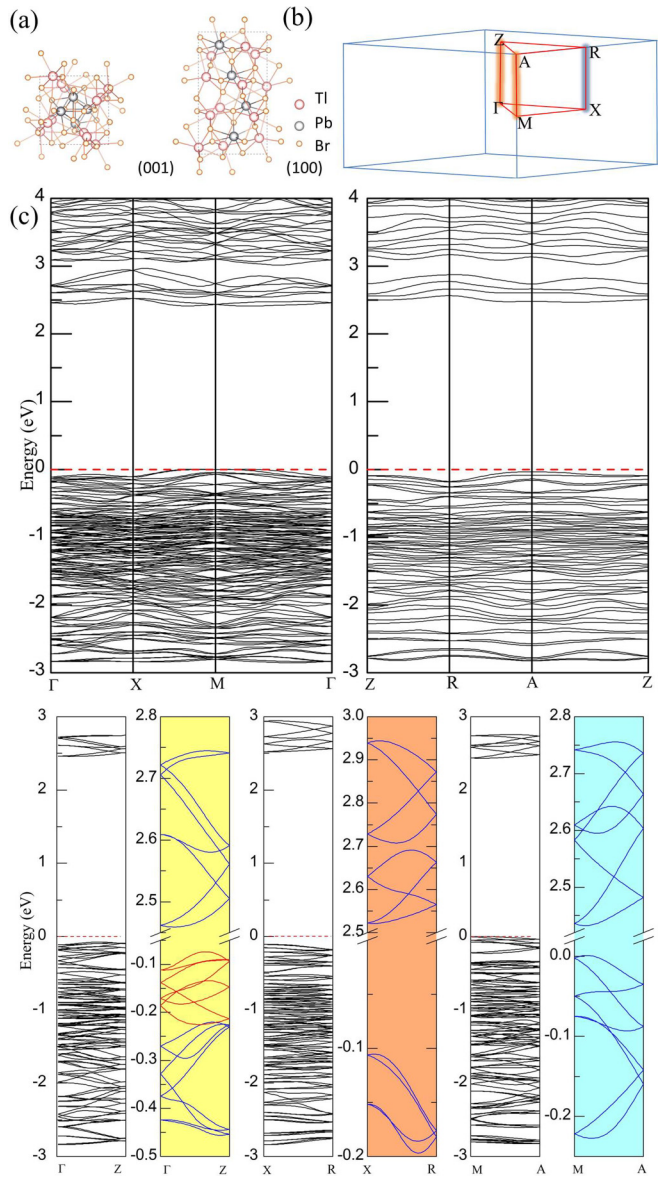

FIG. 9. (a) Crystal structure of Tl_3PbBr_5 in SG $P4_1$. (b) The first BZ and high symmetry points and lines. The fourfold and twofold screw-invariant lines are highlighted by orange and blue, respectively. (c) Band structure of Tl_3PbBr_5 (with SOC). The conduction and valence bands near the Fermi energy showing 4- and 2-hourglass band crossings are enlarged and shown on the right.

Consider SG $P4_1$ first. For nonsymmorphic SGs, the SG representation $D(\{\alpha|\vec{\tau}+\vec{t}\})$ can be obtained from the corresponding point group representations $\Gamma(\{\alpha|0\})$ by $D(\{\alpha|\vec{\tau}+\vec{t}\}) = e^{i\vec{k}\cdot\vec{\tau}}e^{i\vec{k}\cdot\vec{t}}\Gamma(\{\alpha|0\})$. For $\Gamma(0,0,0)$, $\Lambda(0,0,\omega)$, and $Z(0,0,0.5)$ in the BZ, the corresponding point groups—or the group of the $\vec{k}$ vectors are the same, being $\{E, \{C_{2z}|\frac{1}{2}\vec{t}_3\}, \{C_{4z}|\frac{1}{4}\vec{t}_3\}$, and $\{C_{4z}^{-1}|\frac{3}{4}\vec{t}_3\}\}$. Since SOC is considered, the symmetry of bands are described by the double-valued representation [49] of the double SG. The corresponding character table for the double-valued representations of the group of wave vectors at Γ, Λ, and Z are shown in Table II.

From the character table it is obvious that the representations at Γ and Z are both doubly degenerate. This results in the double degeneracy of the bands at Γ and Z, which are both TRIM. Along Λ, the representations are nondegenerate. By comparing the characters of each representation, it is easy to get the following compatibility relations between Γ and Λ,

$$\begin{aligned}\overline{\Gamma}_5\overline{\Gamma}_7 &\to \overline{\Lambda}_5 + \overline{\Lambda}_7,\\ \overline{\Gamma}_6\overline{\Gamma}_8 &\to \overline{\Lambda}_6 + \overline{\Lambda}_8,\end{aligned} \tag{C1}$$

and the compatibility relations between Z and Λ,

$$\begin{aligned}\overline{Z}_5\overline{Z}_5 &\to \overline{\Lambda}_5 + \overline{\Lambda}_5,\\ \overline{Z}_6\overline{Z}_6 &\to \overline{\Lambda}_6 + \overline{\Lambda}_6,\\ \overline{Z}_7\overline{Z}_8 &\to \overline{\Lambda}_7 + \overline{\Lambda}_8.\end{aligned} \tag{C2}$$

The compatibility relations can be schematically shown in Fig. 10(a), which result in the band structure similar to that obtained in the main text by symmetry analysis. We see that each representation has to appear twice to make the set of bands closed, i.e., separated from another set. In Fig. 10(a) they are arranged in such a way to result in a standard 4-hourglass band structure with three crossings along Λ. By tuning the sequence of the representations at Γ or Z we can get a variant of the standard 4-hourglass with more crossings.

Similarly, the double-valued irreducible representations of SG $P3_1$ for the group of wave vectors at Γ, Δ, and A are shown in Table III, from which we have the compatibility relations between Γ and Δ,

$$\begin{aligned}\overline{\Gamma}_4\overline{\Gamma}_4 &\to \overline{\Delta}_4 + \overline{\Delta}_4,\\ \overline{\Gamma}_5\overline{\Gamma}_6 &\to \overline{\Delta}_5 + \overline{\Delta}_6,\end{aligned} \tag{C3}$$

and the compatibility relation between A and Δ,

$$\begin{aligned}\overline{A}_4\overline{A}_6 &\to \overline{\Delta}_4 + \overline{\Delta}_6,\\ \overline{A}_5\overline{A}_5 &\to \overline{\Delta}_5 + \overline{\Delta}_5.\end{aligned} \tag{C4}$$

The compatibility relations are shown schematically in Fig. 10(b), with minimally two crossings along Δ.

TABLE II. The double-valued irreducible representations of SG $P4_1$, for the group of wave vectors at Γ, Z, and Λ. The degeneracy due to TRS for each representation is added at the end of each row, with a and b meaning doubly degenerate and c nondegenerate [50]. Here $0 < \omega < 0.5$. For $\omega = 0$, Λ becomes Γ and for $\omega = 0.5$, Λ becomes Z.

Repres.	E	$\{C_{2z}\|\frac{1}{2}\vec{t}_3\}$	$\{C_{4z}\|\frac{1}{4}\vec{t}_3\}$	$\{C_{4z}^{-1}\|\frac{3}{4}\vec{t}_3\}$	T. I.
$\overline{\Gamma}_5$	1	$-i$	$e^{i\frac{3}{4}\pi}$	$e^{-i\frac{3}{4}\pi}$	b
$\overline{\Gamma}_6$	1	$-i$	$e^{-i\frac{1}{4}\pi}$	$e^{i\frac{1}{4}\pi}$	b
$\overline{\Gamma}_7$	1	i	$e^{-i\frac{3}{4}\pi}$	$e^{i\frac{3}{4}\pi}$	b
$\overline{\Gamma}_8$	1	i	$e^{i\frac{1}{4}\pi}$	$e^{-i\frac{1}{4}\pi}$	b
$\overline{Z}_5$	1	1	-1	1	a
$\overline{Z}_6$	1	1	1	-1	a
$\overline{Z}_7$	1	-1	$-i$	$-i$	b
$\overline{Z}_8$	1	-1	i	i	b
$\overline{\Lambda}_5$	1	$-ie^{i\pi\omega}$	$e^{i\frac{3}{4}\pi}e^{i\frac{1}{2}\pi\omega}$	$e^{-i\frac{3}{4}\pi}e^{i\frac{3}{2}\pi\omega}$	c
$\overline{\Lambda}_6$	1	$-ie^{i\pi\omega}$	$e^{-i\frac{1}{4}\pi}e^{i\frac{1}{2}\pi\omega}$	$e^{i\frac{1}{4}\pi}e^{i\frac{3}{2}\pi\omega}$	c
$\overline{\Lambda}_7$	1	$ie^{i\pi\omega}$	$e^{-i\frac{3}{4}\pi}e^{i\frac{1}{2}\pi\omega}$	$e^{i\frac{3}{4}\pi}e^{i\frac{3}{2}\pi\omega}$	c
$\overline{\Lambda}_8$	1	$ie^{i\pi\omega}$	$e^{i\frac{1}{4}\pi}e^{i\frac{1}{2}\pi\omega}$	$e^{-i\frac{1}{4}\pi}e^{i\frac{3}{2}\pi\omega}$	c

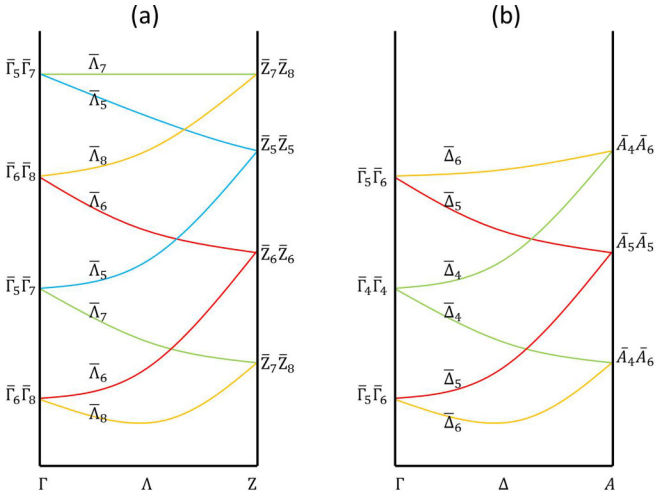

FIG. 10. (a) The compatibility relations between bands at Γ, Λ, and Z of crystals with $P4_1$ SG symmetry. (b) The compatibility relations between bands at Γ, Δ, and A of crystals with $P3_1$ SG symmetry.

APPENDIX D: BAND STRUCTURES WITHOUT SOC

The n-hourglasslike band structures appear in the presence of SOC. In the main text we have pointed out that when SOC is ignored, the n-hourglasslike structures turn into V-like, N-like, and W-like structures for $n = 2, 3, 4$, respectively, using our effective model. Here we give the band structures without SOC and show that the V-, N-, and W-like band structures can also be understood from the compatibility relations between the single-valued irreducible representations of the group of wave vectors.

For SG $P4_1$, the groups of wave vectors at Γ, Z, and Λ are the same with that in Appendix C. The only difference is that now we are concerned with the single-valued irreducible representations [51], which describe the symmetry of bands when the Hamiltonian contains no spin-dependent terms. The results are shown in Table IV, from which we can derive the compatibility relations between irreducible representations of the group of wave vectors at Γ and Λ,

$$\begin{aligned} \Gamma_1 &\to \Lambda_1, \\ \Gamma_2 &\to \Lambda_2, \\ \Gamma_3\Gamma_4 &\to \Lambda_3 + \Lambda_4, \end{aligned} \tag{D1}$$

and the compatibility relations between the irreducible representation at Z and Λ,

$$\begin{aligned} Z_1Z_3 &\to \Lambda_1 + \Lambda_3, \\ Z_2Z_4 &\to \Lambda_2 + \Lambda_4. \end{aligned} \tag{D2}$$

From the compatibility relations, the W-like band structure along ΓZ can be deduced and is shown schematically in Fig. 13(a).

In a similar way we can obtain the single-valued irreducible representation of crystals with $P3_1$ SG symmetry, as shown in Table V, from which the compatibility relations between Γ

TABLE III. Double-valued irreducible representations of SG $P3_1$ for the group of wave vectors at Γ$(0, 0, 0)$, $A(0, 0, 0.5)$, and $\Delta(0, 0, \omega)$ with $0 < \omega < 0.5$. The degeneracy due to TRS for each representation is added at the end of each row, with a and b meaning doubly degenerate and c nondegenerate.

Repres.	E	$\{C_{3z}\|\frac{1}{3}\vec{t}_3\}$	$\{C_{3z}^{-1}\|\frac{2}{3}\vec{t}_3\}$	T. I.
$\overline{\Gamma}_4$	1	-1	-1	a
$\overline{\Gamma}_5$	1	$e^{-i\frac{1}{3}\pi}$	$e^{i\frac{1}{3}\pi}$	b
$\overline{\Gamma}_6$	1	$e^{i\frac{1}{3}\pi}$	$e^{-i\frac{1}{3}\pi}$	b
$\overline{A}_4$	1	$e^{-i\frac{2}{3}\pi}$	$e^{-i\frac{1}{3}\pi}$	b
$\overline{A}_5$	1	1	-1	a
$\overline{A}_6$	1	$e^{i\frac{2}{3}\pi}$	$e^{i\frac{1}{3}\pi}$	b
$\overline{\Delta}_4$	1	$-e^{i\frac{2}{3}\pi\omega}$	$-e^{i\frac{4}{3}\pi\omega}$	c
$\overline{\Delta}_5$	1	$e^{-i\frac{1}{3}\pi}e^{i\frac{2}{3}\pi\omega}$	$e^{i\frac{1}{3}\pi}e^{i\frac{4}{3}\pi\omega}$	c
$\overline{\Delta}_6$	1	$e^{i\frac{1}{3}\pi}e^{i\frac{2}{3}\pi\omega}$	$e^{-i\frac{1}{3}\pi}e^{i\frac{4}{3}\pi\omega}$	c

TABLE IV. The single-valued irreducible representations of SG $P4_1$, for the group of wave vectors at Γ, Z, and Λ. The degeneracy due to TRS for each representation is added at the end of each row, with a meaning nondegenerate and b and c doubly degenerate. Here $0 < \omega < 0.5$. For $\omega = 0$, Λ becomes Γ and for $\omega = 0.5$, Λ becomes Z.

Repres.	E	$\{C_{2z}\|\frac{1}{2}\vec{t}_3\}$	$\{C_{4z}\|\frac{1}{4}\vec{t}_3\}$	$\{C_{4z}^{-1}\|\frac{3}{4}\vec{t}_3\}$	T. I.
Γ_1	1	1	1	1	a
Γ_2	1	1	-1	-1	a
Γ_3	1	-1	i	$-i$	b
Γ_4	1	-1	$-i$	i	b
Z_1	1	i	$e^{i\frac{1}{4}\pi}$	$e^{i\frac{3}{4}\pi}$	b
Z_2	1	i	$e^{-i\frac{3}{4}\pi}$	$e^{-i\frac{1}{4}\pi}$	b
Z_3	1	$-i$	$e^{-i\frac{1}{4}\pi}$	$e^{-i\frac{3}{4}\pi}$	b
Z_4	1	$-i$	$e^{i\frac{3}{4}\pi}$	$e^{i\frac{1}{4}\pi}$	b
Λ_1	1	$e^{i\pi\omega}$	$e^{i\frac{1}{2}\pi\omega}$	$e^{i\frac{3}{2}\pi\omega}$	a
Λ_2	1	$e^{i\pi\omega}$	$-e^{i\frac{1}{2}\pi\omega}$	$-e^{i\frac{3}{2}\pi\omega}$	a
Λ_3	1	$-e^{i\pi\omega}$	$-ie^{i\frac{1}{2}\pi\omega}$	$ie^{i\frac{3}{2}\pi\omega}$	a
Λ_4	1	$-e^{i\pi\omega}$	$ie^{i\frac{1}{2}\pi\omega}$	$-ie^{i\frac{3}{2}\pi\omega}$	a

TABLE V. Single-valued irreducible representations of SG $P3_1$ for the group of wave vectors at Γ$(0, 0, 0)$, $A(0, 0, 0.5)$, and $\Delta(0, 0, \omega)$, with $0 < \omega < 0.5$. The degeneracy due to TRS for each representation is added at the end of each row, with a meaning nondegenerate and b and c doubly degenerate.

Repres.	E	$\{C_{3z}\|\frac{1}{3}\vec{t}_3\}$	$\{C_{3z}^{-1}\|\frac{2}{3}\vec{t}_3\}$	T. I.
Γ_1	1	1	1	a
Γ_2	1	$e^{i\frac{2}{3}\pi}$	$e^{-i\frac{2}{3}\pi}$	b
Γ_3	1	$e^{-i\frac{2}{3}\pi}$	$e^{i\frac{2}{3}\pi}$	b
A_1	1	$e^{i\frac{1}{3}\pi}$	$e^{i\frac{2}{3}\pi}$	b
A_2	1	-1	1	a
A_3	1	$e^{-i\frac{1}{3}\pi}$	$e^{-i\frac{2}{3}\pi}$	b
Δ_1	1	$e^{i\frac{2}{3}\pi\omega}$	$e^{i\frac{4}{3}\pi\omega}$	a
Δ_2	1	$e^{i\frac{2}{3}\pi}e^{i\frac{2}{3}\pi\omega}$	$e^{-i\frac{2}{3}\pi}e^{i\frac{4}{3}\pi\omega}$	a
Δ_3	1	$e^{-i\frac{2}{3}\pi}e^{i\frac{2}{3}\pi\omega}$	$e^{i\frac{2}{3}\pi}e^{i\frac{4}{3}\pi\omega}$	a

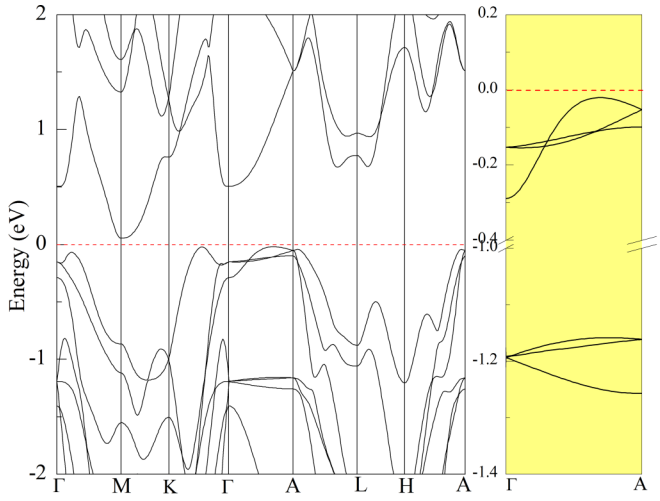

FIG. 11. Band structure of HgTe without SOC. The valence bands near Fermi energy showing N-like dispersions are enlarged and shown on the right.

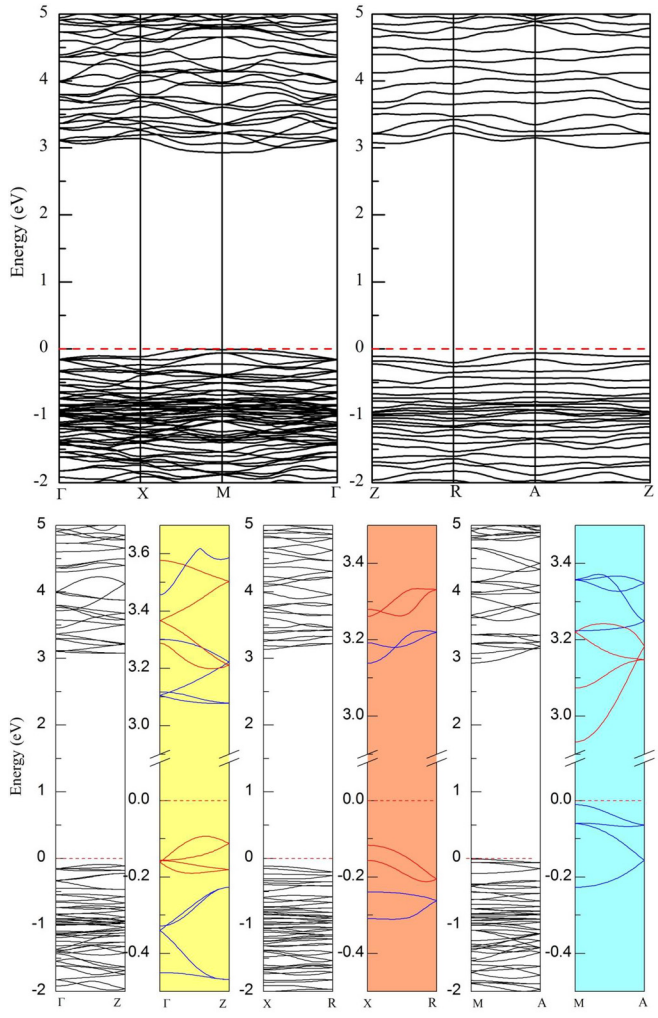

FIG. 12. Band structure of Tl_3PbBr_5 without SOC. The conduction and valence bands near Fermi energy showing W-like dispersions are enlarged and shown on the right of each screw-invariant path.

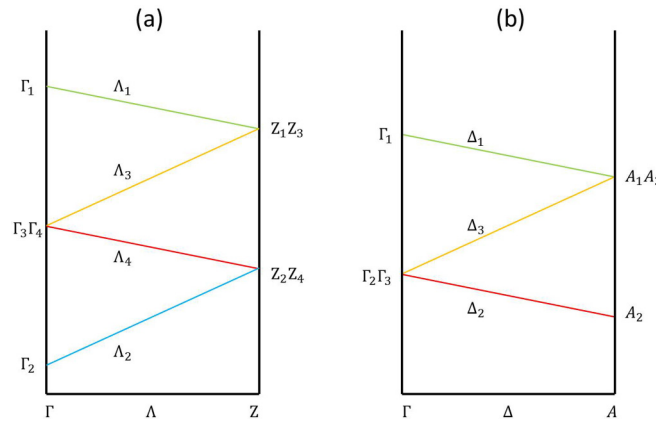

FIG. 13. (a) The compatibility relations between bands at Γ, Λ, and Z of crystals with $P4_1$ SG, ignoring SOC. (b) Compatibility relation for bands at Γ, Δ, and A of crystals with $P3_1$ SG, also ignoring SOC.

and Δ,

$$\begin{aligned}\Gamma_1 &\to \Delta_1,\\ \Gamma_2\Gamma_3 &\to \Delta_2+\Delta_3,\end{aligned} \tag{D3}$$

and the compatibility relations between A and Δ,

$$\begin{aligned}A_1A_3 &\to \Delta_1+\Delta_3,\\ A_2 &\to \Delta_2,\end{aligned} \tag{D4}$$

are obtained. The N-like band structures along ΓA can be deduced, as shown in Fig. 13(b).

The band structures of HgTe and Tl_3PbBr_5 without SOC are shown in Figs. 11 and 12, respectively. For HgTe, along the screw-invariant line (ΓA), the band structure shows N-like dispersion, similar to that shown in Fig. 13(b). The shape can vary due to permutations of the vertices at Γ and A as well as curving. Similarly, for Tl_3PbBr_5, along ΓZ and MA, the band structure show W-like dispersions as in Fig. 13(a). Along XR, which is a twofold screw-invariant line, the bands show V-like dispersion. In the whole plane ZRA the bands are doubly degenerate, due to the presence of a twofold screw axis [11].

APPENDIX E: TIGHT-BINDING MODEL WITH A THREEFOLD SCREW AXIS

In this Appendix we write a tight-binding model with a threefold screw symmetry and TRS, which at the screw-invariant lines reduces to the effective model presented in the main text. We start with a quasi-1D spinless system with a threefold screw symmetry shown in Fig. 14(a), which resides on a helix. There are three sites in each unit cell, with the z-direction coordinate mc, $(m+\frac{1}{3})c$, and $(m+\frac{2}{3})c$, respectively, where m is an integer and c is the lattice constant in z direction. Their projections onto the xy plane form an equilateral triangle. We repeat the 1D system to generate the 3D lattice, of which the projection on the xy plane is shown in Fig. 14(b). There are three sublattices indicated by three different colors. Each sublattice has a layered structure, with each layer being a triangle lattice. Let the lattice constant

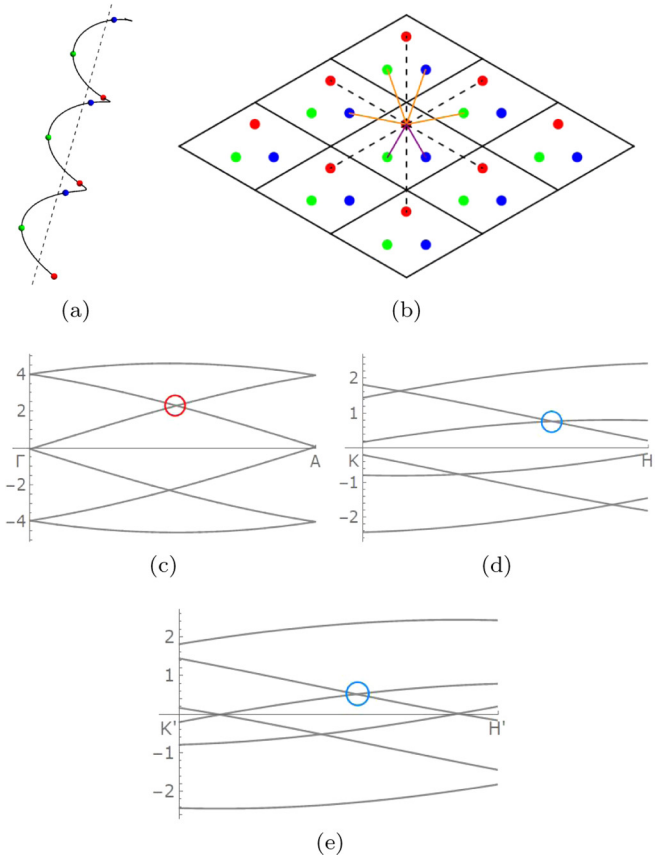

FIG. 14. (a) A quasi-1D system with a threefold screw symmetry. All the dots are regarded as the same atoms, while different colors indicate different sublattices. The system lies on a helix which has a continuous screw symmetry. The screw axis is indicated by the dashed line. (b) The tight-binding lattice composed of the quasi-1D system (a). All hopping processes considered are illustrated for one site. The purple solid lines represent the hopping t_0 and the associated SOC λ_0, the black dashed lines t_1 and λ_1 and λ_2, and the orange solid lines t_2 and $\lambda_0\beta$. (c)–(e) The band structure along ΓA, KH, and $K'H'$, respectively. The tight-binding parameters are $t_0 = 1, t_2 = 0.5$, $\lambda_0 = 0.8$, $\lambda_1 = 0.3$, $\lambda_2 = 0.1$, and $\beta = 0.2$.

in the xy plane be a, then the primitive vectors are $\mathbf{a}_1 = (\frac{\sqrt{3}}{2}a, -\frac{1}{2}a, 0)$, $\mathbf{a}_2 = (\frac{\sqrt{3}}{2}a, \frac{1}{2}a, 0)$, and $\mathbf{a}_3 = (0, 0, c)$, and the reciprocal primitive vectors are $\mathbf{b}_1 = \frac{2\pi}{a}(\frac{\sqrt{3}}{3}, -1, 0)$, $\mathbf{b}_2 = \frac{2\pi}{a}(\frac{\sqrt{3}}{3}, 1, 0)$, and $\mathbf{b}_3 = \frac{2\pi}{c}(0, 0, 1)$. We include three types of hopping in our tight-binding model, indicated by the three types of lines in Fig. 14(b): purple solid lines for out-of-plane nearest-neighbor hopping t_0, black dashed lines for in-plane nearest-neighbor hopping t_1, and orange solid lines for out-of-plane next-nearest-neighbor hopping t_2. The tight-binding Hamiltonian without SOC $H_0(\mathbf{k})$ has elements

$$\begin{aligned}(H_0)_{\text{diag}} &= 2t_1 \sum_{i=1}^{3} \cos \mathbf{k}\cdot\boldsymbol{\delta}_i,\\ (H_0)_{12} &= t_0 + t_2(e^{i\mathbf{k}\cdot\boldsymbol{\delta}_2} + e^{-i\mathbf{k}\cdot\boldsymbol{\delta}_3}),\\ (H_0)_{13} &= t_0 e^{ik_z c} + t_2 e^{ik_z c}(e^{-i\mathbf{k}\cdot\boldsymbol{\delta}_1} + e^{i\mathbf{k}\cdot\boldsymbol{\delta}_2}),\\ (H_0)_{23} &= t_0 + t_2(e^{-i\mathbf{k}\cdot\boldsymbol{\delta}_1} + e^{i\mathbf{k}\cdot\boldsymbol{\delta}_3}),\end{aligned} \tag{E1}$$

where $\boldsymbol{\delta}_i$'s are defined as $\boldsymbol{\delta}_1 = \mathbf{a}_1$, $\boldsymbol{\delta}_2 = \mathbf{a}_2 - \mathbf{a}_1$, and $\boldsymbol{\delta}_3 = -\mathbf{a}_2$. The diagonal terms $(H_0)_{\text{diag}}$ do not affect the band crossings, so we will set $t_1 = 0$ for simplicity. Other nonzero elements are determined by the Hermitian condition. The time-reversal operator is $T = K$ where K represents the complex conjugation. The TRS is expressed as

$$TH_0(\mathbf{k})T^{-1} = H_0(-\mathbf{k}), \tag{E2}$$

and the eight TRIM are $\frac{1}{2}\sum_{i=1}^{3}(n_i\mathbf{b}_i)$ with $n_i = 0$ or 1. The screw operation is represented by

$$S_3 = \begin{pmatrix} 0 & 0 & e^{ik_z c} \\ 1 & 0 & 0 \\ 0 & 1 & 0 \end{pmatrix}. \tag{E3}$$

H_0 has the screw symmetry

$$S_3 H_0(\mathbf{k}) S_3^{\dagger} = H_0\left[R_z\left(\frac{2\pi}{3}\right)\mathbf{k}\right], \tag{E4}$$

where $R_z(\theta)$ represents rotation about the z axis by θ clockwise, and $R_z(\frac{2\pi}{3})\mathbf{k} = (-\frac{1}{2}k_x + \frac{\sqrt{3}}{2}k_y, -\frac{\sqrt{3}}{2}k_x - \frac{1}{2}k_y, k_z)$.

When spin is taken into account, the time-reversal operation becomes $T = i\sigma_y K$ and the screw operation becomes $S_3' = S_3 \otimes e^{i\frac{\pi}{3}\sigma_z}$. The SOC term must satisfy

$$TH_{\text{SO}}(\mathbf{k})T^{-1} = H_{\text{SO}}(-\mathbf{k}) \tag{E5}$$

and

$$S_3' H_{\text{SO}}(\mathbf{k}) S_3'^{\dagger} = H_{\text{SO}}\left[R_z\left(\frac{2\pi}{3}\right)\mathbf{k}\right]. \tag{E6}$$

The term associated with the out-of-plane nearest-neighbor and next-nearest-neighbor hopping is given by

$$H_{\text{SO}}^{(1)} = \lambda_0 i(A - A^{\dagger}) \otimes \sigma_z, \tag{E7}$$

where the nonzero elements of A are

$$\begin{aligned}A_{13} &= e^{ik_z c}[1 + \beta(e^{-i\mathbf{k}\cdot\boldsymbol{\delta}_1} + e^{i\mathbf{k}\cdot\boldsymbol{\delta}_2})],\\ A_{21} &= 1 + \beta(e^{-i\mathbf{k}\cdot\boldsymbol{\delta}_2} + e^{i\mathbf{k}\cdot\boldsymbol{\delta}_3}),\\ A_{32} &= 1 + \beta(e^{i\mathbf{k}\cdot\boldsymbol{\delta}_1} + e^{-i\mathbf{k}\cdot\boldsymbol{\delta}_3}).\end{aligned} \tag{E8}$$

Along screw-invariant lines, $H_{\text{SO}}^{(1)}$ reduces to the SOC term of the effective model in the main text. This term combined with H_0 gives rise to the 3-hourglass band structure along the k_z axis, but the crossings reside on nodal lines. To get Weyl points, we need more symmetry-allowed terms to break those additional degeneracies. We include two SOC terms associated with the in-plane nearest-neighbor hopping,

$$H_{\text{SO}}^{(2)} = \lambda_1\left(\sum_i \sin \mathbf{k}\cdot\boldsymbol{\delta}_i\right)\mathcal{I}_3 \otimes \sigma_z \tag{E9}$$

and

$$H_{\text{SO}}^{(3)} = \lambda_2\left(\sum_i \sin \mathbf{k}\cdot\boldsymbol{\delta}_i\right)\begin{pmatrix} M_\theta & & \\ & M_{\theta-\frac{2\pi}{3}} & \\ & & M_{\theta+\frac{2\pi}{3}} \end{pmatrix}, \tag{E10}$$

where $M_\theta = \sigma_x \cos\theta + \sigma_y \sin\theta$ which satisfies

$$e^{i\frac{\pi}{3}\sigma_z} M_\theta e^{-i\frac{\pi}{3}\sigma_z} = M_{\theta-\frac{2\pi}{3}}. \tag{E11}$$

The $\mathbf{k}$-dependent factor is invariant under threefold screw rotation. $H_{\text{SO}}^{(2)}$ and $H_{\text{SO}}^{(3)}$ preserve both screw symmetry and

TRS. We may include more symmetry-allowed hopping and SOC terms, but for the purpose of finding the Weyl points it is enough to have these terms. The band structure is plotted along ΓA, KH, and $K'H'$ in Figs. 14(c), 14(d), and 14(e), respectively. Along ΓA, the bands form a 3-hourglass. We focus on the crossings between the second and the third highest band. The symmetry-enforced crossing along ΓA is labeled by a red circle, and the symmetry-indirectly-enforced crossings along KH and $K'H'$ by blue circles. This realizes the $3+3$ case discussed in the main text, and coincides with the case of HgTe in cinnabar phase.

[1] M. Z. Hasan and C. L. Kane, Rev. Mod. Phys. **82**, 3045 (2010).
[2] X.-L. Qi and S.-C. Zhang, Rev. Mod. Phys. **83**, 1057 (2011).
[3] A. P. Schnyder, S. Ryu, A. Furusaki, and A. W. W. Ludwig, Phys. Rev. B **78**, 195125 (2008).
[4] A. Kitaev, in *Advances in Theoretical Physics: Landau Memorial Conference*, edited by V. Lebedev and M. Feigel'man, AIP Conf. Proc No. 1134 (AIP, New York, 2009), p. 22.
[5] L. Fu, Phys. Rev. Lett. **106**, 106802 (2011).
[6] B. Bradlyn, J. Cano, Z. Wang, M. G. Vergniory, C. Felser, R. J. Cava, and B. A. Bernevig, Science **353** aaf5037 (2016).
[7] H. Watanabe, H. C. Po, M. P. Zaletel, and A. Vishwanath, Phys. Rev. Lett. **117**, 096404 (2016).
[8] K. Shiozaki, M. Sato, and K. Gomi, Phys. Rev. B **93**, 195413 (2016).
[9] Z. Wang, A. Alexandradinata, R. J. Cava, and B. A. Bernevig, Nature (London) **532**, 189 (2016).
[10] S. M. Young and C. L. Kane, Phys. Rev. Lett. **115**, 126803 (2015).
[11] L. Wang, S.-K. Jian, and H. Yao, Phys. Rev. B **96**, 075110 (2017).
[12] A. Furusaki, Sci. Bull. **62**, 788 (2017).
[13] Y. Chen, H.-S. Kim, and H.-Y. Kee, Phys. Rev. B **93**, 155140 (2016).
[14] R. Takahashi, M. Hirayama, and S. Murakami, Phys. Rev. B **96**, 155206 (2017).
[15] T. Bzdusek, Q. Wu, A. Rüegg, M. Sigrist, and A. A. Soluyanov, Nature (London) **538**, 75 (2016).
[16] S.-S. Wang, Y. Liu, Z.-M. Yu, X.-L. Sheng, and S. A. Yang, Nat. Commun. **8**, 1844 (2017).
[17] B. Singh, B. Ghosh, C. Su, H. Lin, A. Agarwal, and A. Bansil, Phys. Rev. Lett. **121**, 226401 (2018).
[18] B. Fu, X. Fan, D. Ma, C.-C. Liu, and Y. Yao, Phys. Rev. B **98**, 075146 (2018).
[19] W. Wu, Y. Liu, S. Li, C. Zhong, Z.-M. Yu, X.-L. Sheng, Y. X. Zhao, and S. A. Yang, Phys. Rev. B **97**, 115125 (2018).
[20] J. Zhang, Y.-H. Chan, C.-K. Chiu, M. G. Vergniory, L. M. Schoop, and A. P. Schnyder, Phys. Rev. Mater. **2**, 074201 (2018).
[21] N. P. Armitage, E. J. Mele, and A. Vishwanath, Rev. Mod. Phys. **90**, 015001 (2018).
[22] W. Setyawan and S. Curtarolo, Comput. Mater. Sci. **49**, 299 (2010).
[23] H. Nielsen and M. Ninomiya, Nucl. Phys. B **185**, 20 (1981).
[24] J. Ruan, S.-K. Jian, H. Yao, H. Zhang, S.-C. Zhang, and D. Xing, Nat. Commun. **7**, 11136 (2016).
[25] J. Ruan, S.-K. Jian, D. Zhang, H. Yao, H. Zhang, S.-C. Zhang, and D. Xing, Phys. Rev. Lett. **116**, 226801 (2016).
[26] L. Wang, S.-K. Jian, and H. Yao, Phys. Rev. A **93**, 061801(R) (2016).
[27] A. H. Castro Neto, F. Guinea, N. M. R. Peres, K. S. Novoselov, and A. K. Geim, Rev. Mod. Phys. **81**, 109 (2009).
[28] Y. Wang and P. Ye, Phys. Rev. B **94**, 075115 (2016).
[29] I. Sodemann and L. Fu, Phys. Rev. Lett. **115**, 216806 (2015).
[30] Q. Ma, S.-Y. Xu, H. Shen, D. MacNeill, V. Fatemi, T.-R. Chang, A. M. Mier Valdivia, S. Wu, Z. Du, C.-H. Hsu, S. Fang, Q. D. Gibson, K. Watanabe, T. Taniguchi, R. J. Cava, E. Kaxiras, H.-Z. Lu, H. Lin, L. Fu, N. Gedik, and P. Jarillo-Herrero, Nature (London) **565**, 337 (2018).
[31] F.-Y. Li, Y.-D. Li, Y. B. Kim, L. Balents, Y. Yu, and G. Chen, Nat. Commun. **7**, 12691 (2016).
[32] L. Lu, Z. Wang, D. Ye, L. Ran, L. Fu, J. D. Joannopoulos, and M. Soljačić, Science **349**, 622 (2015).
[33] Y. H. Chan, B. Kilic, M. M. Hirschmann, C.-K. Chiu, L. M. Schoop, D. G. Joshi, and A. P. Schnyder, Phys. Rev. Mater. **3**, 124204 (2019).
[34] B. Bradlyn, L. Elcoro, J. Cano, M. G. Vergniory, Z. Wang, C. Felser, M. I. Aroyo, and B. A. Bernevig, Nature (London) **547**, 298 (2017).
[35] M. G. Vergniory, L. Elcoro, Z. Wang, J. Cano, C. Felser, M. I. Aroyo, B. A. Bernevig, and B. Bradlyn, Phys. Rev. E **96**, 023310 (2017).
[36] E. R. Scheinerman and D. H. Ullman, *Fractional Graph Theory* (John Wiley & Sons, New York, 2008).
[37] B. Joshi, A. Thamizhavel, and S. Ramakrishnan, Phys. Rev. B **84**, 064518 (2011).
[38] Z. Sun, M. Enayat, A. Maldonado, C. Lithgow, E. Yelland, D. C. Peets, A. Yaresko, A. P. Schnyder, and P. Wahl, Nat. Commun. **6**, 6633 (2015).
[39] A. Werner, H. D. Hochheimer, K. Strössner, and A. Jayaraman, Phys. Rev. B **28**, 3330 (1983).
[40] N. G. Wright, M. I. McMahon, R. J. Nelmes, and A. San-Miguel, Phys. Rev. B **48**, 13111 (1993).
[41] T.-J. Hu, X.-Y. Cui, X.-F. Li, J.-S. Wang, X.-M. Lv, L.-S. Wang, J.-H. Yang, and C.-X. Gao, Chin. Phys. B **24**, 116401 (2015).
[42] S. Radescu, A. Mujica, J. López-Solano, and R. J. Needs, Phys. Rev. B **83**, 094107 (2011).
[43] O. Khyzhun, V. Bekenev, O. Parasyuk, S. Danylchuk, N. Denysyuk, A. Fedorchuk, N. AlZayed, and I. Kityk, Opt. Mater. **35**, 1081 (2013).
[44] N. Denysyuk, V. Bekenev, M. Karpets, O. Parasyuk, S. Danylchuk, and O. Khyzhun, J. Alloys Compd. **576**, 271 (2013).
[45] G. Kresse and J. Furthmüller, Phys. Rev. B **54**, 11169 (1996).
[46] P. E. Blöchl, Phys. Rev. B **50**, 17953 (1994).
[47] J. P. Perdew, K. Burke, and M. Ernzerhof, Phys. Rev. Lett. **77**, 3865 (1996).
[48] H. J. Monkhorst and J. D. Pack, Phys. Rev. B **13**, 5188 (1976).
[49] L. Elcoro, B. Bradlyn, Z. Wang, M. G. Vergniory, J. Cano, C. Felser, B. A. Bernevig, D. Orobengoa, G. de la Flor, and M. I. Aroyo, J. Appl. Crystallogr. **50**, 1457 (2017).
[50] C. Herring, Phys. Rev. **52**, 361 (1937).
[51] M. Tinkham, *Group Theory and Quantum Mechanics* (Dover, New York, 2003).